Eur. Phys. J. A **6**, 157–165 (1999)

THE EUROPEAN PHYSICAL JOURNAL A

Nuclear shell gaps at finite temperatures

C. Reiß[1], M. Bender[2,3], P.-G. Reinhard[1,4]

[1] Institut für Theoretische Physik II, Universität Erlangen-Nürnberg, Staudtstrasse 7, 91058 Erlangen, Germany
[2] Department of Physics and Astronomy, The University of North Carolina, Chapel Hill, NC 27516–3255, USA
[3] Department of Physics and Astronomy, The University of Tennessee, Knoxville, TN 37996, USA
[4] Joint Institute for Heavy–Ion Research, Oak Ridge National Laboratory, P. O. Box 2008, Oak Ridge, TN 37831, USA

Received: 29 September 1998 / Revised version: 1 July 1999
Communicated by F. Lenz

Abstract. Neutron–rich nuclei with a closed neutron shell represent chains of waiting–point nuclei in the astrophysical r–process. Details of their nuclear structure like separation energies, shell structure and β^-–decay half–lives have a dramatic influence on element abundances calculated from r–process simulations. Actual supernova scenarios take place at finite temperature. To investigate the influence of finite temperature on binding energies and shell gaps, i.e. the second derivative of the binding energy, we calculate the shell gaps in the range of interest and slightly beyond, i.e. $0 \leq k_{\rm B}T \leq 0.8$ MeV. Basis of the description is the self–consistent Skyrme–Hartree–Fock model and an extension of BCS pairing to finite temperature using a natural orbital representation.

PACS. 21.60.Jz Hartree-Fock and random-phase approximations – 21.60.-n Nuclear-structure models and methods

1 Introduction

Models for the nucleosynthesis in astrophysical objects predict that the formation of most heavy nuclei with masses $A > 60$ occurs in nature in two distinct neutron–capture processes, the s–process in red giants and the r–process which takes place in supernovae [1–4]. The production rates and final abundances of the various elements depend, of course, crucially on the properties of the involved nuclei, most of all on their binding energies and β^-–decay half–lives. While the s–process stays fairly close to the valley of stability, the r–process moves through the region of β^-–unstable nuclei far away from stability, most of them still experimentally unavailable, although there is some recent progress for the identification [5] and the measurement of some of the β^-–decay properties [6] of some r–process nuclei near the $N = 50$ neutron shell, where the r–process path comes close to the stability line.

Thus r–process simulations need to rely on theoretical input for the necessary nuclear physics information. It turns out that various available nuclear mean–field models, both self–consistent ones and more phenomenological approaches like the macroscopic–microscopic models, still provide much different predictions for the abundances [7] and there is presently much activity to pin down the nuclear models more precisely in order to enhance their predictive power. All of such considerations up to now have dealt with information from the nuclear ground state. Actual r–process scenarios, however, take place at finite temperatures in the range of typically $0.1 < k_{\rm B}T < 0.4$ MeV [8]. It is the aim of this paper to investigate the effect of finite temperature on nuclear binding energy systematics.

More specifically, we are going to investigate the temperature dependence of the nuclear binding energy and derived observables, i.e. the two–nucleon separation energy and the two–nucleon shell gap. The latter quantities play a crucial role in determining the abundances, particularly near neutron shell closures which constitute a chain of "waiting–point" nuclei responsible for the r–process peaks in the element abundances [7].

As basis for the description, we take the Skyrme–Hartree–Fock (SHF), for an early review see [9], complemented with the BCS pairing model. This is a self–consistent, non–relativistic nuclear mean–field model which is very successful in describing bulk properties of stable nuclei, see e.g. [10]. The model can be used safely for finite temperatures if they are not too large [11], and we are here certainly on the safe side when we consider temperatures below 1 MeV. In fact, SHF at finite temperatures has been investigated several times before [12–14], but with much different bias, mainly concerned with the breakdown of shell structure at higher $k_{\rm B}T \approx 2\,$MeV [12, 13] or with equilibrium in the presence of a dense neutron vapor [14]. The aim here is to look at lower temperatures and at effects which are, at first glance, less obvious, but which turn out at the end to be important for the stellar scenarios.

The paper is outlined as follows: In Sect. 2, we present the formal framework of our mean–field+BCS treatment at finite temperature. In Sect. 3, we present and discuss the results considering as test cases the tin isotopes and the $N = 82$ isotones.

2 Formal framework

2.1 The energy functionals

The investigation requires first an extension of the standard SHF+BCS treatment to finite temperatures. This was already done in [13] using finite temperature HFB cranking with Surface Delta Interaction in a two level model with total isospin 0 and 1. We prefer, however, a variational formulation in terms of natural orbitals, similar as it has been used for zero temperature in [15]. This gives simpler access to the pairing equations in case of more general pairing functionals as we use it here. And it is particularly convenient in connection with codes where the wavefunctions are represented on a grid in coordinate space.

The formal derivations take as starting point an effective energy functional of the form

$$E = E_{\rm mf}[\underbrace{\rho,\tau,\mathcal{J}}_{\hat\rho}] + E_{\rm pair}[\chi] - E_{\rm c.m.} \quad , \tag{1}$$

that is the sum of the mean–field energy functional $E_{\rm mf}$, the pairing energy functional $E_{\rm pair}$ and the correction for spurious center–of–mass motion $E_{\rm c.m.}$. For the mean–field functional $E_{\rm mf}[\hat\rho]$ we employ the Skyrme energy functional which can be formulated in terms of the local density ρ, local kinetic energy density τ, and local spin–orbit current $\mathcal{J}$. As we are here not interested in unfolding all details of this rather elaborate functional [16], we abbreviate the dependence with the most general case, the full one–body density matrix

$$\hat\rho \equiv \rho(\mathbf{r}\sigma,\mathbf{r}'\sigma') = \langle\hat\psi^\dagger(\mathbf{r}',\sigma')\hat\psi(\mathbf{r},\sigma)\rangle \quad . \tag{2}$$

For the present purposes, it suffices to know that the functional variation yields the mean–field Hamiltonian

$$\hat h_{\rm mf} = \frac{\delta E_{\rm mf}}{\delta\hat\rho} \quad . \tag{3}$$

More formal details can be found, e.g., in [16]. We will use actually the parameterizations SkT6 [17], SkI4 [18], as well as SLy4 [19] and postpone a brief summary of their features at the beginning of Sect. 3.

The pairing functional used in this investigation

$$E_{\rm pair}[\chi] = \frac{1}{4}\sum_{q\in p,n} V_{{\rm pair},q}\int {\rm d}^3r\ \chi_q^*(\mathbf{r})\,\chi_q(\mathbf{r}) \quad , \tag{4}$$

can be derived from a local, two–body like–particle pairing interaction $V_{{\rm pair},q}\,\delta(\mathbf{r}-\mathbf{r}')$ [20,21]. Note that the pairing energy functional decouples in the sum of separate contributions from protons and neutrons. Therefore the pairing and mean–field equations will decouple as well into equations for protons and neutrons. We will omit the isospin index in the following. The pairing functional depends on the local part of the pair density χ only

$$\chi(\mathbf{r}) = \sum_{\sigma=\pm1}(-\sigma)\langle\hat\psi(\mathbf{r},-\sigma)\hat\psi(\mathbf{r},\sigma)\rangle \quad . \tag{5}$$

The variation of the pairing energy functional with respect to χ yields the pairing potential

$$\Delta(\mathbf{r}) = \frac{\delta E_{\rm pair}}{\delta\chi(\mathbf{r})} \tag{6}$$

which turns out to be a local potential for the present form of the pairing functional. The mean–field Hamiltonian $\hat h_{\rm mf}$ and the pairing potential Δ do not necessarily commute with each other. The BCS approximation forces commensurability in that it considers only those elements of Δ which are diagonal in the eigenbasis of $\hat h_{\rm mf}$. The corresponding approximative steps follow in the course of the further derivation.

Finally we have to take care of the center-of-mass correction and it is to be done with the same recipe as was used when designing the forces. Thus in case of SkI4, we subtract

$$E_{\rm c.m.} = \frac{\langle\hat{\mathbf{P}}^2_{\rm c.m.}\rangle}{2m_{\rm N}A} \quad . \tag{7}$$

after variation, i.e. after having solved the variational mean–field equations (to avoid the costly treatment of a two-body operator during variation). The actual computation of this expectation value has to be revised in view of the mix of temperature and pairing, for details see appendix A. In case of SkT6 and SLy4, we consider only the diagonal part of the correction, i.e. $\hat{\mathbf{P}}^2_{\rm c.m.} \longrightarrow \sum_i \hat{\mathbf{p}}_i^2$, which amounts to change the nucleon mass as $m \longrightarrow m - m/A$ [9].

2.2 Energy functionals at finite temperature

The energy functional (1) is the correct starting point for a variational formulation at zero temperature. At finite temperature T, one should invoke the Gibbs' free energy $E - \lambda N - TS$ instead. We resolve that here in a two–step process. First we consider a given mean–field and determine the appropriate grand canonical ensemble associated with it (which essentially means to maximize the entropy). This provides an expression of the densities in terms of wavefunctions, pairing amplitudes, and temperature. These are inserted then into the energy functional (1) and the equations for φ_α and v_α are determined variationally, see [22] for a discussion in the framework of the Hartree–Fock model without pairing.

The one–body density matrix and the and local pairing density are still calculated from (2) and (5), but the brackets mean now quantum mechanical expectation value *and*

ensemble average at finite temperature T. The standard steps of BCS theory at finite temperature yield then for the one–body density matrix

$$\rho(\mathbf{r},\sigma;\mathbf{r}',\sigma') = \sum_{\alpha\gtrless 0} n_\alpha\, \varphi_\alpha(\mathbf{r},\sigma)\varphi^*_\alpha(\mathbf{r}',\sigma') \qquad (8)$$

where the n_α are the occupation probabilities determined by the pairing correlations and the finite temperature

$$n_\alpha = \frac{1}{1+\exp\{\beta e_\alpha\}} + \tanh\left\{\frac{\beta e_\alpha}{2}\right\} v_\alpha^2 \quad . \qquad (9)$$

The pair density in a thermal ensemble emerges as

$$\chi(\mathbf{r}) = -2\sum_{\alpha>0} \chi_\alpha\, |\varphi_\alpha(\mathbf{r})|^2 \qquad (10)$$

where the χ_α are the pair occupation probabilities determined by the pairing correlations and the finite temperature

$$\chi_\alpha = \tanh\left\{\frac{\beta e_\alpha}{2}\right\} u_\alpha v_\alpha f_\alpha \quad . \qquad (11)$$

The factor f_α therein regulates the space of single particle states which is active in pairing. It contains the quasiparticle energy which is defined as

$$e_\alpha = (\varepsilon_\alpha - \lambda)\left(u_\alpha^2 - v_\alpha^2\right) + 2\,\Delta_\alpha f_\alpha u_\alpha v_\alpha \quad . \qquad (12)$$

For the selection of this pairing phase space we use a smoothened Woods–Saxon cut–off factor

$$f_\alpha = \frac{1}{1+\exp\{(\varepsilon_\alpha - \lambda - \Delta E)/\mu\}} \quad . \qquad (13)$$

The parameters μ and ΔE are determined self–consistent with

$$\mu = \frac{\Delta E}{10} \quad , \qquad (14)$$

$$N_{\rm act} = N + 1.65N^{2/3} = \sum_{\alpha\gtrless 0} f_\alpha \qquad (15)$$

where $N_{\rm act}$ is the number of effective pairing states and N the number of nucleons [23].

These expressions (8) and (10) are to be inserted into the energy functional (1) which provides then the implicit dependence on the single–particle states φ_α and the pairing amplitudes v_α (with the dependent amplitudes $u_\alpha = \sqrt{1-v_\alpha^2}$) on the temperature. The optimal wavefunctions and amplitudes are to be determined by minimization of of the total energy (1) with a constraint on particle number. During this variation, we neglect the implicit dependence of the phase space cut-off (13) on $\varphi^\dagger_\alpha$ and v_α because possible contributions therefrom are very small. Variation with respect to $\varphi^\dagger_\alpha$ yields

$$\Big((\hat h_{\rm mf} - \lambda)n_\alpha + \underbrace{\chi_\alpha \Delta(\mathbf{r})}_{\approx 0}\Big)\varphi_\alpha(\mathbf{r}) = \sum_{\beta\gtrless 0} \lambda_{\alpha\beta}\,\varphi_\beta(\mathbf{r}) \quad . \qquad (16)$$

As in case of zero temperature, the BCS approximation is obtained by neglecting the contribution from the pairing energy functional the left–hand–side of [23]. Within this approximation, $\lambda_{\alpha\beta}$ can be diagonalized by a unitary transformation of the single–particle wavefunctions with the eigenvalues $n_\alpha(\varepsilon_\alpha - \lambda)$ leading to the familiar equation-of–motion

$$\hat h_{\rm mf}\varphi_\alpha = \varepsilon_\alpha \varphi_\alpha \quad . \qquad (17)$$

The generalized gap equation is obtained from variation of the particle–number constrained energy functional with respect to v_α^2

$$\left(\varepsilon_\alpha - \lambda - \frac{\Delta_\alpha f_\alpha(1-2v_\alpha^2)}{2\sqrt{v_\alpha^2(1-v_\alpha^2)}}\right) = \underbrace{\frac{\beta e_\alpha}{2\,\sinh\{\beta e_\alpha\}}\frac{\partial e_\alpha}{\partial v_\alpha^2}}_{\approx 0} \qquad (18)$$

where $\varepsilon_\alpha = (\varphi_\alpha|\hat h_{\rm mf}|\varphi_\alpha)$ are the diagonal matrix elements of the single–particle Hamiltonian and e_α is the quasiparticle energy as defined in (12). The right–hand–side accesses the residual interactions in the mean–field and gap potentials. It accounts for the linear response of the energy functionals to the thermal change of the occupation. We expect this to be a small effect and neglect the response terms in the present treatment. Within that approximation we then obtain the standard form of the gap equation which can be resolved as usual, yielding

$$v_\alpha^2 = \frac{1}{2}\left(1 - \frac{\varepsilon_\alpha - \lambda}{\sqrt{(\varepsilon_\alpha-\lambda)^2 + f_\alpha^2\Delta_\alpha^2}}\right) \quad . \qquad (19)$$

The thermal BCS scheme in natural orbitals φ_α thus requires only minimal modifications as compared to the formalism at zero temperature. One merely needs to account for the thermal factors in collecting the densities $\hat\rho$ and $\chi(\mathbf{r})$, see (8) and (10).

The numerical solution then proceeds as in the case of zero temperature. Actually, we are considering here spherical nuclei and compute the radial wavefunctions on a coordinate–space grid using five–point finite differences to define the derivate operators, for details see [24].

3 Results and discussion

For this first exploration, we have confined the considerations to spherical nuclei which basically restricts the pool of examples to semi–magic systems. Systematic scans over the various possible chains of isotopes and isotones yield all very similar effects. It thus suffices to present here the results for one test case. The most interesting aspect for the r–process are the two-neutron separation energies and shell gap for the isotones with neutron number $N = 82$. We will present results for these isotones. Before coming to that, however, we want to discuss the temperature effects as such. This will be done in two steps. First, we discuss the interplay of pairing and temperature, and second, we

investigate the temperature effects on separation energies and shell gap for the chain of Sn isotopes as test case.

There exists a puzzling manifold of Skyrme forces (we found about 80 in the literature) from which we have to select a few typical ones. We present here results for the three parameterizations SkT6 [17], SkI4 [18], and SLy4 [19]. All these parameterizations have been obtained from fits to nuclear ground–state data, binding energies, radii, and a few selected spin–orbit splittings. The fit of force SkI4 included even the whole electromagnetic formfactor at low q (i.e. up to the first maximum). All three forces provide a very good description of the gross properties of the stable nuclei and share the basic nuclear matter properties as binding $E/A = -16\,\mathrm{MeV}$, equilibrium density $\rho_0 = 0.16\,\mathrm{fm}^{-3}$, incompressibility $230\,\mathrm{MeV} \leq K \leq 250\,\mathrm{MeV}$, asymmetry energy $30\,\mathrm{MeV} \leq a_4 \leq 32\,\mathrm{MeV}$, and a low sum rule enhancement factor $0 \leq \kappa \leq 0.25$. The main differences lie in the effective mass, the less prominent isovector features, and in the spin–orbit coupling. The more recent forces SkI4 and Sly4 have rather low effective mass $0.65 \leq m^*/m \leq 0.69$ whereas SkT6 kept strictly the bare nucleon mass, i.e. $m^*/m = 1$. The forces SkT6 and SLy4 employ the standard spin–orbit coupling as derived from a zero–range two-body spin–orbit force [9] whereas SkI4 accesses an extended spin–orbit functional which was inspired by the relativistic mean field model and which aims at a more flexible isovector part of the spin–orbit force [18]. Both, the effective mass as well as the spin–orbit splitting, have a strong influence on the actual level densities and are thus important parameters for the temperature effects to be studied. The three forces in the sample cover the most typical variants, low versus high effective mass and standard versus extended spin–orbit splitting. There are, furthermore, differences in the details of the isovector coupling leading, e.g. to somewhat different density dependence of a_4 and different surface asymmetry. The effect of these subtle details on shell closures and extrapolations to exotic nuclei has not yet been sufficiently explored. It is probably not very pronounced such that the present variation of m^*/m and of spin–orbit coupling suffices.

3.1 Basic features of thermal BCS — gaps and phase transition

A paired state is a phase which appears only at low temperatures. With increasing T, there comes a sudden breakdown of pairing. For a quantitative demonstration, one usually parameterizes pairing by the pairing gap for which we take here the average spectral gap [23]

$$\langle \Delta \rangle = \frac{\sum_{\alpha>0} f_\alpha \, v_\alpha u_\alpha \, \Delta_\alpha}{\sum_{\alpha>0} f_\alpha \, u_\alpha v_\alpha} \quad . \tag{20}$$

The evolution of pairing with increasing temperature is demonstrated in Fig. 1 where we show the average neutron pair gap $\langle \Delta \rangle$ for the chain of tin isotopes. For the mean–field energy functional, the parameterization SkI4 from [18] is employed. The curves $\langle \Delta(T) \rangle$ show the same

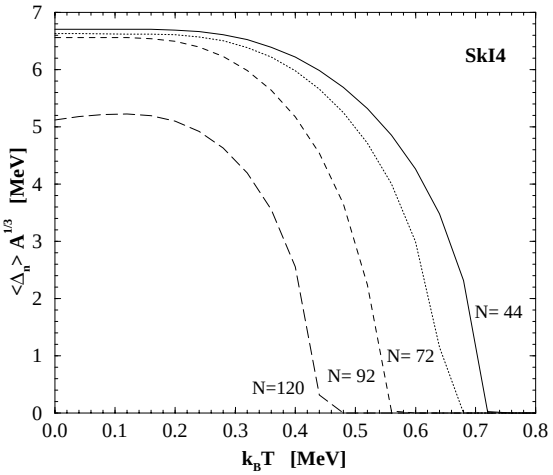

Fig. 1. The temperature dependence of the average neutron pair gap $\langle \Delta_n \rangle$ scaled with $A^{1/3}$ for four different tin isotopes as indicated. The parameterization SkI4 has been used for the underlying mean–field

pattern for all temperatures as they are well known since long for the BCS pairing gap, see e.g. [25]. The gap resists heating for a while and then disappears rather quickly at a critical temperature T_c. So the overall pattern follows in all cases a universal curve. What differs, however, in the different isotopes is the actual value for T_c. But that is not too surprising. The pairing gap at $T = 0$ depends sensitively on the density of single–particle levels in the vicinity of the Fermi surface and thus depends on the actual neutron and proton numbers. A smaller gap at zero temperature translates then into a lower T_c by virtue of the universal behavior of $\langle \Delta(T) \rangle$.

Figure 1 gives the impression as if the average pair gap would systematically decrease with increasing neutron number. Although this is true as a general trend, it is an incomplete view in detail. The more systematic information is provided in Fig. 2 where we show the average pairing gaps at $T = 0$ and the critical temperatures for Sn–isotopes versus neutron number. In addition to SkI4 which was used in the previous figure, we also present results for the two other mean–field parameterizations in the sample, namely SkT6 and SLy4. The strong variations with neutron number are obvious. Pairing breaks down complete at the neutron shell closures and reaches a maximum in the mid–shell region. As one can deduce from the previous Fig. 1, the critical temperature should closely follow the trends of the average gap, and that is nicely corroborated in Fig. 2. The different mean–field parameterizations, however, predict different trends in details. The pairing gaps in the mid–shell region $50 < N < 82$ do not follow a simple inverted parabola, but show substructure which is related to fluctuations in the level density that are related to the details of the single–particle energies. These fluctuations proceed differently for the different forces. Particularly SkI4 shows a double peak structure with a region of reduced level density around $N = 68$. The differences become even more amplified when going into the regime of neutron–rich isotopes. There the forces even predict shell

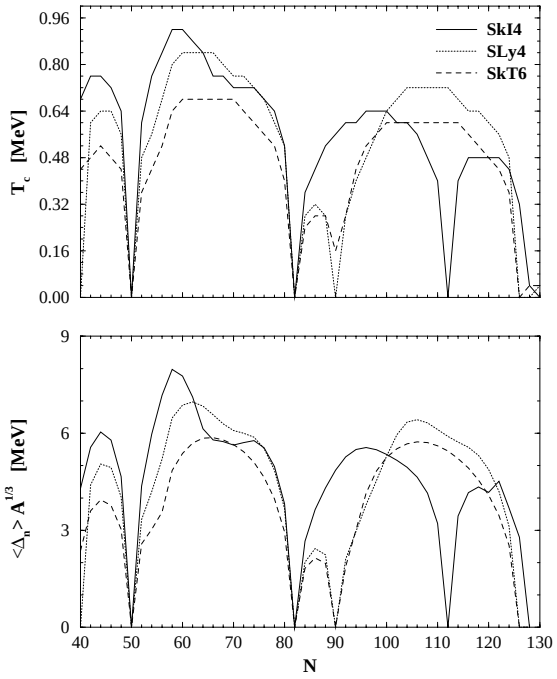

Fig. 2. The lower panel shows the average neutron pair gap $\langle \Delta_n \rangle$ at $T = 0$ and scaled with $A^{1/3}$ for tin isotopes and for three different of mean–field parameterizations as indicated. The upper panel shows the corresponding critical temperatures T_c

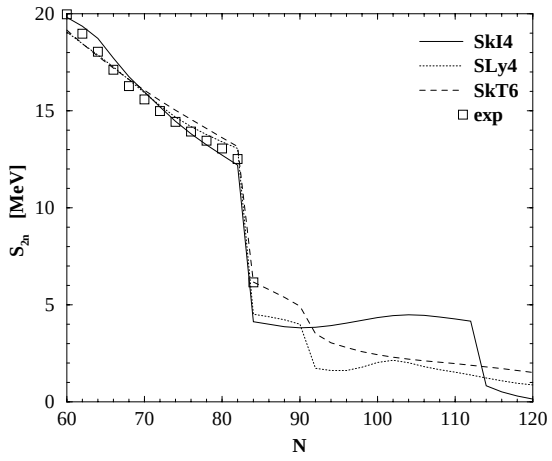

Fig. 3. The two–neutron separation energy S_{2n} at zero temperature for the chain of tin isotopes and a selection of mean–field parameterizations as indicated, compared with experimental values where available

closures at different neutron numbers. The forces SkT6 and SLy4 agree an a magic $N = 90$ whereas SkI4 prefers the very neutron–rich $N = 112$. These varying predictions are related to the fact that any one of these shell closures is less well developed than the standard magic numbers. Tiny changes can then have a large effect. We see, moreover, that the pairing gap is rather small in the small mid–shell region $82 < N < 90$. This altogether lets us expect that temperature effects will be more pronounced in the region of neutron–rich isotopes. The force SkT6 displays a curious detail at $N = 90$ which demonstrates once more that this is a interesting region where the shell structure is somewhat fluctuating. The average gap (lower panel) looks as if there were a shell closure. But the critical temperature does not really drop down to zero. In fact, we find for the average gap at $N = 90$ the small, but non–zero, value $\langle \Delta_n \rangle A^{1/3} = 0.1$. There is thus a very low level density but the gap is just not large enough to call it a subshell closure.

3.2 Two–neutron separation energies

The most prominent observables for nuclei are binding energies and differences thereof. For example, the two neutron separation energy

$$S_{2n}(Z,N) = E_B(Z,N-2) - E_B(Z,N) \qquad (21)$$

characterizes the isotopic trends of the energy, hints on the stability of a nucleus. Before going to temperature effects on this quantity, we need to look at the typical results from nowadays mean–field parameterizations for this observable. Figure 3 shows the S_{2n} for the Sn isotopes computed with the three Skyrme forces SkT6, SLy4, and SkI4. All three forces provide a very good description of the nuclear bulk properties along the valley of stability. This can also be seen from Fig. 3 where all three forces agree nicely with the experimental values for $N \leq 82$. But the extrapolation towards the neu-tron–rich isotopes comes out very different. The size of the jump of S_{2n} at $N = 82$ is much smaller for SkT6 than for the two other forces. This feature is related to the different effective masses: SkT6 uses $m^*/m = 1$ whereas SLy4 and SkI4 employ rather low values $m^*/m \approx 0.7$. The further evolution is also different. SkT6 and SLy4 have a faint shell closure at $N = 90$ as indicated by the small jump in the S_{2n} there, whereas SkI4 waits with the next closure until $N = 112$.

Figure 3 has demonstrated the typical variations of nowadays mean–field models when extrapolated to neu-tron–rich nuclei. These differences have an impact on the predicted abundances in the r–process and the actual discussion is much concerned with getting more reliable theoretical predictions in this regime. But one needs to take into account the fact that the actual r–processes take place at a finite temperature of $0.1 \leq k_B T \leq 0.4$ MeV, and the question is which variations in the S_{2n} are produced when changing the temperature. Figure 4 shows the S_{2n} at various temperatures. There emerge indeed visible changes, particularly at the side of the exotic nuclei ($N \geq 82$). The step to 0.2 MeV temperature makes still very little effect. But from then on, one can have substantial changes which could affect a quantitative analysis of stellar abundances. In particular, we see that the changes often have different sign below and above shell closure which will influence effects related to shell closure more than visible from the S_{2n} here.

Another dramatic effect is seen towards $N \approx 96$. Although the temperature effects as such may look small,

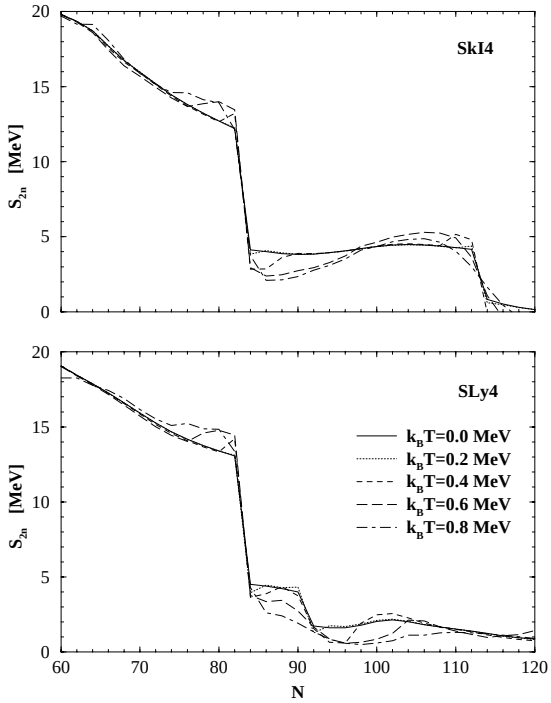

Fig. 4. The two–neutron separation energy S_{2n} for tin isotopes at several finite temperatures as indicated and for two different mean–field parameterizations (upper panel: SkI4, lower panel: SLy4)

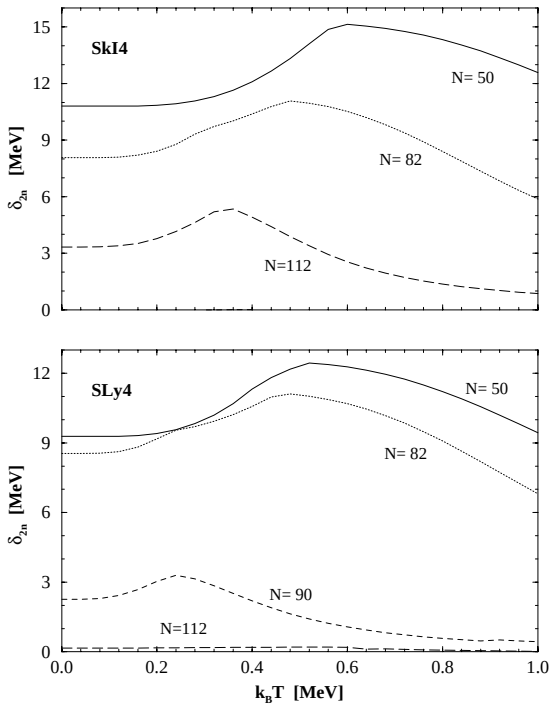

Fig. 5. The temperature dependence of the two neutron shell gap at shell closures for Sn isotopes and for the two Skyrme parameterization SkI4 (upper panel) and SLy4 (lower panel)

they drive here the S_{2n} very close to zero and thus destabilize these nuclei. The point is that the change of S_{2n} with temperature has about the same magnitude everywhere. But the relative effect can grow huge if the S_{2n} as such are small which is the case, of course, when going to very neutron rich systems.

3.3 Two–neutron shell gaps

The most interesting points appear at shell closures which constitute the chains of waiting–point nuclei that are important for the explanation of the final r–process abundances. The "closeness" of a shell can be quantified in terms of the two–nucleon shell gap which represents the size of the jump of the S_{2n}. It is thus the first difference of the S_{2n} and the second difference of the binding energies. Here we consider the second difference of the binding energies, i.e. the two–neutron shell gap

$$\delta_{2n} = E_B(Z, N+2) - 2E_B(Z, N) + E_B(Z, N-2). \quad (22)$$

We now have one number to characterize each shell closure. This allows to draw the trends with temperature which is, of course, more informative then looking at few selected points. Figure 5 shows the $\delta_{2n}(T)$ at neutron shell closures for the two Skyrme forces SkI4 and SLy4.One sees here in detail that the results stay indeed stable up to $k_{\rm B}T = 0.2$ MeV and start to vary quickly after that point. The effects on the δ_{2n} can obviously grow large even for moderate temperatures. Consider, e.g., the shell gap at $N = 82$ and compare the change from zero to 0.3 MeV temperature (which is a possible value in stellar scenarios): the variation comes out to be 1–1.5 MeV just as large as the varying predictions for different Skyrme forces. The effect is even more important for the fainter shell closures in the regime of exotic nuclei.

At first glance, one may be surprised that the shell gap starts with increasing as function of T while one would have expected a destabilization of the nuclei when heating. The nuclei are indeed less well bound if T grows. But a closed–shell nucleus is more robust against this change than its neighbors and this increases first the second difference (22). The mechanism is demonstrated in Fig. 6 which shows temperature dependence of the binding energies around shell closure. It obvious that the magic $N = 82$ comes latest to feel the temperature. This then gives rise to the observed initial increase of δ_{2n}. It is only if the closed shell nucleus reacts to T which happens at 0.5 MeV that the shell gap bends over to a steady decrease.

Figure 7 looks at the two-neutron shell gaps from a different perspective. Concentrating on the $N = 82$ closure, the isotonic trends of the shell gap are shown for a selection of temperatures. The upper panel shows the two-neutron separation energies and serves as a protocol of the stability of the isotones. Decreasing Z for fixed N drives the samples deeper into the regime of exotic nuclei, and the S_{2n} shrinks correspondingly. Here we find 0.1 MeV as the temperature up to which nothing changes. The step to 0.2 MeV already degrades the stability visibly and moves the drip line by two units. The next step to 0.4 MeV induces a further large reduction of S_{2n} for the heavier sys-

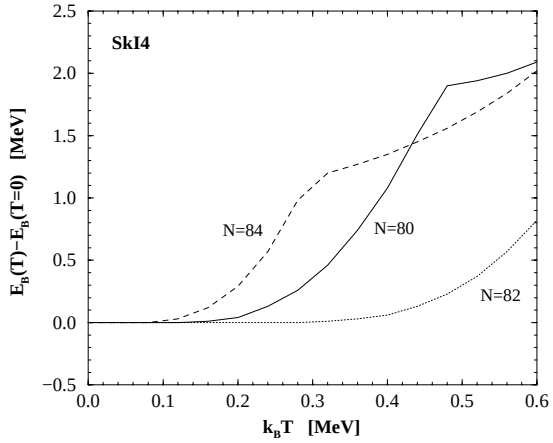

Fig. 6. The temperature dependence binding energies $E_{\rm B}$ for ^{130}Sn, ^{132}Sn and ^{134}Sn drawn relative to $E_{\rm B}$ at $T = 0$. These results have been computed with the mean–field parameterization SkI4

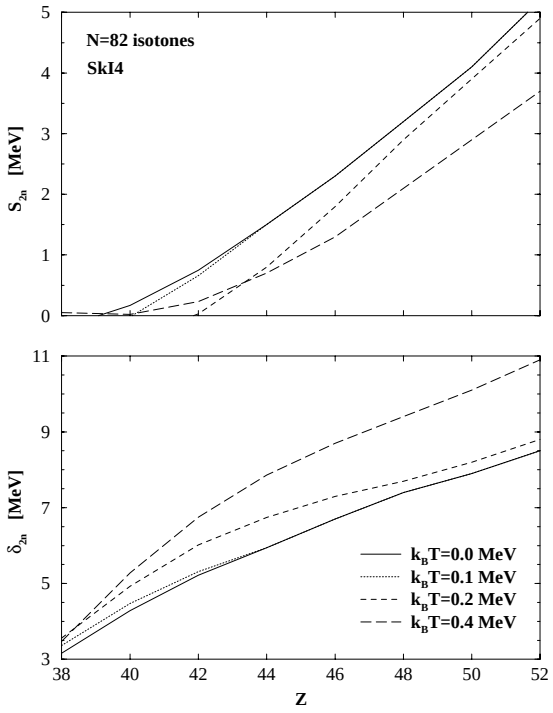

Fig. 7. Lower panel: The isotonic trend of the two–neutron shell gap $\delta_{2n}(Z, 82)$ for various temperatures as indicated and computed with the Skyrme force SkI4. Upper panel: The corresponding $S_{2n}(Z, 82)$

tems, but does less (and can even revert the effect) near the drip-line. This is related to the breakdown of pairing which reduces for a while the amount of continuum nucleons and thus enhances stability. It is known, on the other hand, that the BCS approximation exaggerates the occupation of continuum states and that a full HFB treatment would perform more reasonably in that respect. So we see again in our consideration at finite temperature T what has been found before at $T = 0$ that full HFB is needed near the neutron drip–line [26]. The lower panel of Fig. 7 shows the isotonic trends of δ_{2n} at various temperatures. It is obvious that temperature effects become increasingly important when moving away from the valley of stability (which means here in direction of decreasing Z) such that large effects emerge already at a temperature of $k_{\rm B}T = 0.2$ MeV.

3.4 Tail of the density distribution

Thus far we have discussed energies which are the crucial observables defining the equilibrium distribution of nuclei. The detailed dynamics of the r–process depends also on reaction cross sections and it is interesting to estimate the possible temperature effects there. A cross section is dominated by the overall extension of the nucleus. We have thus looked at the temperature dependence of the radii and find no effect. Strong interaction processes may, however, be already sensitive to the outer tail of the density distribution. To check the effect out there, we show in Fig. 8 the neutron densities for three exotic Sn–isotopes on a logarithmic scale. It requires either a very exotic nucleus ($N = 120$) or rather large temperature ($k_{\rm B}T \geq 0.48$ MeV) to see any sizeable effect. Thus one can probably neglect temperature effects on the reaction rates. The dominant effect is related to the energies.

4 Summary and conclusions

We have considered the effect of small temperatures ($k_{\rm B}T < 1$ MeV) on the predictions of the Skyrme–Hartree–Fock model for binding energies, two–neutron separation energies and two–neutron shell gaps. The BCS scheme is extended to finite temperatures using a representation in terms of natural orbitals. This delivers a formulation where only minimal modifications of existing SHF+BCS codes are required. As test case, we presented mainly the chain of Sn isotopes with an excursion to isotones with neutron number $N = 82$. We find that temperature influences the two–neutron separation energies once it exceeds $k_{\rm B}T = 0.2$ MeV. The effects go in different directions below and above shell closures such that more dramatic temperature dependences are seen for the two–neutron shell gaps. The shell gaps can easily be enhanced by as much as 2 MeV when going from 0 to 0.4 MeV. Such an effect will have an impact on astrophysical calculations of nuclear abundances. We also tried to estimate the effect on reaction cross section by looking at the change of the nuclear density distribution. There are only minimal effects on this observable.

We thank our colleagues J. Engel, T. Bürvenich, K. Rutz, J. A. Maruhn, and W. Haxton for helpful discussions. This work was supported by Bundesministerium für Bildung und Forschung (BMBF), Project No. 06 ER 808, by NATO travel grant, by the U.S. Department of Energy under Contract No. DE–FG02–97ER41019 with the University of North Carolina

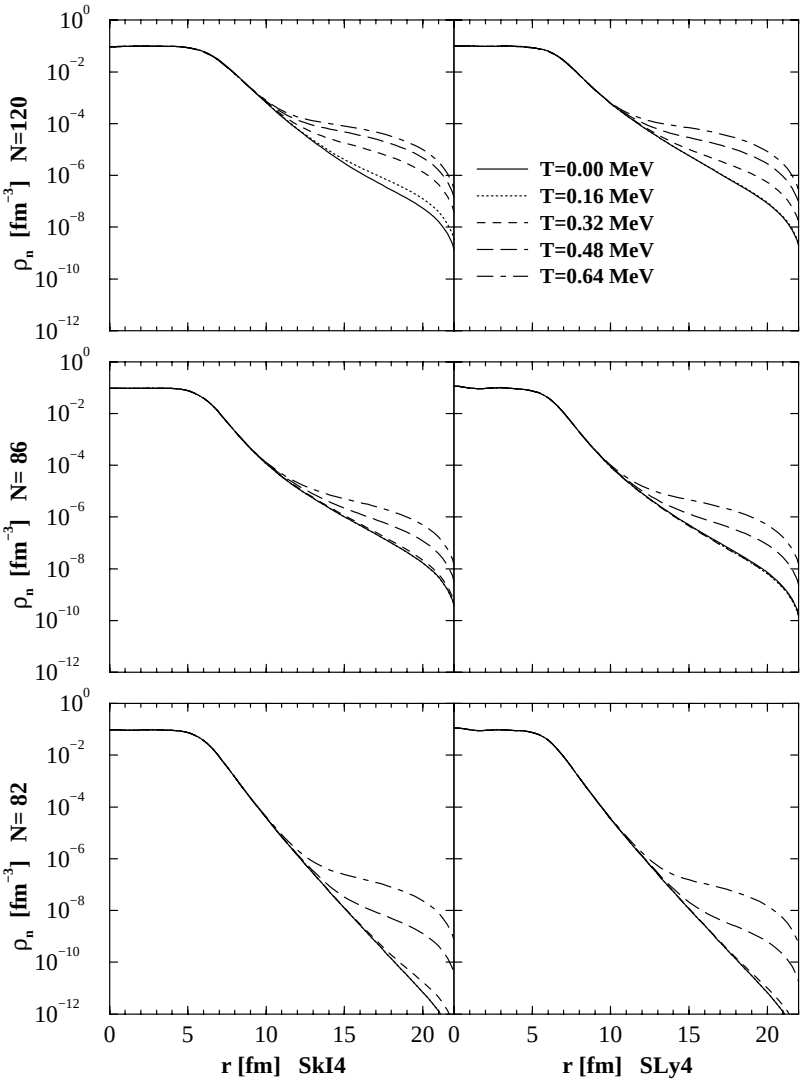

Fig. 8. Neutron densities $\varrho_{\rm n}$ for neutron–rich tin isotopes at various temperatures as indicated. The left column shows results from the force SkI4 and the right from SLy4. The logarithmic scale has been used to pronounce the outer tail of the density distribution

and Contract No. DE–FG02–96ER40963 with the University of Tennessee. The Joint Institute for Heavy Ion Research has as member institutions the University of Tennessee, Vanderbilt University, and the Oak Ridge National Laboratory; it is supported by the members and by the Department of Energy through Contract No. DE–FG05–87ER40361 with the University of Tennessee.

A Correction for center–of–mass motion

The correction for spurious center–of–mass motion (7) cannot be reduced to the densities $\hat{\rho}$ and χ. We need to compute from scratch the thermal expectation value of the center-of-mass fluctuations. It becomes

$$\langle\hat{\mathbf{P}}^2_{\rm c.m.}\rangle = \sum_{\alpha\beta>0} \mathbf{P}^2_{\alpha\beta}\,(u_\alpha v_\beta - v_\alpha u_\beta)^2 \left(\frac{1}{1+e^{\beta e_\alpha}}\frac{1}{1+e^{\beta e_\beta}} + \frac{e^{\beta e_\alpha}}{1+e^{\beta e_\alpha}}\frac{e^{\beta e_\beta}}{1+e^{\beta e_\beta}}\right) \quad . \tag{23}$$

The summation therein runs over all conceivable single–particle state. But we carry explicitly only those states which have non–vanishing occupation v^2_α. It is thus necessary to rearrange the terms using the closure relations such that only occupied wavefunctions appear in the sum. This is achieved by

$$\begin{aligned}\langle\hat{\mathbf{P}}^2_{\rm c.m.}\rangle = {} & 2\sum_{\beta>0}\left(\mathbf{P}^2\right)_\beta\, v^2_\beta(1-w_\beta) \\ & -2\sum_{\alpha\beta>0}\mathbf{P}^2_{\alpha\beta}\Big[v^2_\beta w_\alpha(1-w_\beta) \\ & +\left(v^2_\alpha v^2_\beta + u_\alpha v_\beta v_\alpha u_\beta\right)(1-w_\alpha)(1-w_\beta)\Big] \\ & +2\sum_{\alpha\beta>0}\mathbf{P}^2_{\alpha\beta}\,(u_\alpha v_\beta - v_\alpha u_\beta)^2\, w_\alpha w_\beta \end{aligned} \tag{24}$$

where $w_\alpha = 1/\left(1+e^{\beta e_\alpha}\right)$ the thermal occupation weight

is. The infinite summation over all unoccupied states is then hidden in the matrix element of $\hat{\mathbf{P}}^2_{\mathrm{c.m.}}$, first term on the right hand side.

References

1. E. M. Burbidge, G. R. Burbidge, W. A. Fowler, F. Hoyle, Rev. Mod. Phys. **29**, 547 (1957)
2. D. D. Clayton, *Principles of stellar evolution and nucleosynthesis*, (University of Chicago Press, Chicago, 1983)
3. G. J. Mathews, J. J. Cowan, Nature **345**, 491 (1990)
4. J. K. Cowan, F.–K. Thielemann, J. W. Truran, Phys. Rep. **208**, 267 (1991)
5. Ch. Engelmann, F. Ameil, P. Armbruster, M. Bernas, S. Czajkowski, Ph. Dessagne, C. Dinzaud, H. Geissel, A. Heinz, Z. Janas, C. Kozhuharov, Ch. Miehé, G. Münzenberg, M. Pfützner, C. Röhl, W. Schwab, C. Stéphan, K. Sümmerer, L. Tassan–Got, B. Voss, Z. Phys. A**352**, 251 (1995)
6. F. Ameil, M. Bernas, P. Armbruster, S. Czajkowski, Ph. Dessagne, H. Geissel, E. Hanelt, C. Kozhuharov, C. Miehé, C. Donzaud, A. Grewe, A. Heinz, Z. Janas, M. de Jong, W. Schwab, S. Steinhäuser, Eur. Phys. J. A**1**, 275 (1998)
7. B. Chen, J. Dobazcewski, K.–L. Kratz, K. Langanke, B. Pfeiffer, F.–K. Thielemann, P. Vogel, Phys. Lett. **B355**, 37 (1995)
8. Y.–Z. Qian, W. C. Haxton, K. Langanke, P. Vogel, Phys. Rev. C **55**, 1532 (1997)
9. P. Quentin, H. Flocard, Ann. Rev. Nucl. Part. Sci. **28**, 523 (1978)
10. P. Ring, P. Schuck, *The Nuclear Many–Body Problem*, (Springer, Heidelberg, 1980)
11. J. Cugnon, A. Lejeune, M. Baldo, U. Lombardo, Nucl. Phys. **A492**, 173 (1989)
12. M. Brack, P. Quentin, Nucl. Phys. **A361**, 35 (1981)
13. K. Mühlhans, Eva M. Müller, U. Mosel and A. L. Goodman Z. Phys. A**313**, 133 (1983)
14. P. Bonche, S. Levit, D. Vautherin, Nucl. Phys. **A427**, 278 (1984)
15. P.–G. Reinhard, M. Bender, K. Rutz, and J. A. Maruhn, Z. Phys. A**358**, 277 (1997)
16. P.–G. Reinhard, Ann. Phys. (Leipzig) **1**, 632 (1992)
17. F. Tondeur, M. Brack, M. Farine, J. M. Pearson, Nucl. Phys. **A420**, 297 (1984)
18. P.–G. Reinhard, H. Flocard, Nucl. Phys. **A584**, 467 (1995)
19. E. Chabanat, Ph. D. thesis, Lyon, 1995; E. Chabanat, P. Bonche, P. Haensel, J. Meyer, R. Schaeffer, Nucl. Phys. **A635**, 231 (1998)
20. F. Tondeur, Nucl. Phys. **A315**, 353 (1979)
21. S. J. Krieger, P. Bonche, H. Flocard, P. Quentin, and M. S. Weiss, Nucl. Phys. **A517**, 275 (1990)
22. D. Vautherin, Advances in Nuclear Physics **22**, 123 (1996)
23. M. Bender, P.–G. Reinhard, K. Rutz, and J. A. Maruhn, submitted to Phys. Rev. C (1998)
24. P.–G. Reinhard, in *Computational Nuclear Physics I – Nuclear Structure*, edited by K. Langanke, S. E. Koonin, and J. A. Maruhn, (Springer, Berlin 1991)
25. C. Kittel, *Quantum Theory of Solids*, (John Wiley and Sons, New York, 1963)
26. J. Dobaczewski, W. Nazarewicz, T. R. Werner, J. F. Berger, C. R. Chinn, and J Dechargé, Phys. Rev. C **53**, 2809 (1996)